Energy-Efficient Low-Complexity CMOS Pulse Generator for Multiband UWB Impulse Radio

Anh Tuan Phan, *Associate Member, IEEE*, Jeongseon Lee, Vladimir Krizhanovskii, Quan Le, Seok-Kyun Han, and Sang-Gug Lee, *Member, IEEE*

***Abstract*—This paper presents an energy-efficient low-complexity pulse-generator design technique for multiband impulse-radio ultrawide-band (IR-UWB) system in 0.18-μm CMOS technology. The short pulses are generated based on the on/off switching operation of an oscillator with subband switching functionality, which is mandatory for multiband IR-UWB systems. The relation between the oscillator switching operation and the resulting output pulse envelope, which determines pulse spectral characteristics, is analyzed, and the design guidelines for topology and component values are presented. Measurements show the output pulses with the duration of 3.5 ns, which corresponds to 520-MHz bandwidth. The output pulse spectrum centered at 3.8 GHz fully complies with the Federal Communication Commission spectral mask with more than 25 dB of sidelobe suppression without the need for additional filtering. Thus, the low-complexity pulse generator can maintain its simplicity for low cost with core chip size of 0.3 mm^2. The pulse generator shows an excellent energy efficiency with average energy dissipation of 16.8 pJ per pulse from 1.5-V supply. The proposed pulse generator is best suited for energy-detection IR-UWB systems.**

***Index Terms*—CMOS, Federal Communication Commission (FCC) spectral mask, impulse radio, low power, pulse generator, transmitter, ultrawide-band (UWB).**

I. Introduction

ULTRAWIDE-BAND (UWB), which is regulated for commercial use of the band 3.1–10.6 GHz by the Federal Communication Commission (FCC), has recently emerged as a promising technology for short-range wireless data communications [1]. In impulse-radio (IR-UWB) approach which uses short-duration impulses modulated in time, polarity is attractive for low-cost low-power low-data-rate wireless-communication applications such as RF Tag [2], wireless sensor network [3], and wireless body area network [4]. IR-UWB has also drawn much attention from the researchers as well as industries with a number of advantages including robustness to multipath fading, lower interferences to existing communication systems, and precise localization capability due to the very short pulse nature. By IEEE 802.15.4a Task Group [5], IR-UWB has been chosen as a candidate to deliver communications and high-precision ranging. Moreover, the IR-UWB system can operate in burstlike scheme with low duty cycle, short active period, and long sleep period, leading to a substantial reduction in power consumption.

So far, several works have been reported to develop IR-UWB transceivers. There are two data demodulation schemes for IR-UWB system, coherent and noncoherent demodulations. The coherent transceiver reported in [6] is highly complex and contains the problem of precise timing synchronization between transmitter and receiver. The noncoherent transceivers proposed in [7] and [8] avoid the need for complex synchronization blocks. The noncoherent transceiver is more attractive as a low-power low-complexity solution despite the drawback of being susceptible to noise and interference. This paper applies for the noncoherent scheme.

Fig. 1 shows a noncoherent IR-UWB transceiver proposed by this paper as a low-complexity, low-power, and low-cost solution. In Fig. 1, only the pulse generator and a modulator are used in the transmitter to generate short pulses that are emitted by UWB antenna at low FCC-compliant output power level. The receiver includes a wideband LNA [9], an analog correlator, and an ADC. The correlator shown in Fig. 1 can be implemented as a multiplier combining an integrator using analog technique for simplicity and low-power solution. Considering the low-data-rate ($\sim$100 kbit/s) applications of IR-UWB system, the proposed architecture can adopt the simple on–off keying (OOK) modulation. Therefore, the analog correlator and the ADC in the receiver as well as the pulse generator in the transmitter can operate with the same low-frequency clock. Hence, the output of the correlator that comes to the ADC is slow in speed, relaxing the ADC design.

This paper presents the design and implementation of an energy-efficient low-complexity CMOS pulse generator suitable for the noncoherent multiband IR-UWB architecture shown in Fig. 1. In the remainder of the paper, Section II provides an overview of various UWB pulses, circuit techniques, and the limitations. Section III presents the pulse-generation principle with theoretical analysis. Section IV describes the pulse-generator topologies that can accommodate the proposed pulse structure and the design details. Section V provides experimental results of the implemented pulse generator, and Section VI concludes.

II. Pulse-Generation Challenges

A. Requirements

Typical IR-UWB systems operate in a single channel over the whole UWB band of 3.1–10.6 GHz, which is interfered by other

Manuscript received June 28, 2007, revised March 4, 2008. First published May 20, 2008; current version published December 12, 2008. This work was supported by the Korea Science and Engineering Foundation (KOSEF) grant funded by the Korea gobernment (MEST) (R0A-2007-000-10050-0). This paper was recommended by Associate Editor B. Zhao.

A. T. Phan, J. Lee, V. Krizhanovskii, S.-K. Han, and S.-G. Lee are with the μ-Radio Laboratory, Information and Communications University, Daejeon 305-732 Korea (e-mail: anh@icu.ac.kr).

Q. Le is with the Electronics and Telecommunications Research Institute, Daejeon 305-350, Korea.

Digital Object Identifier 10.1109/TCSI.2008.925821

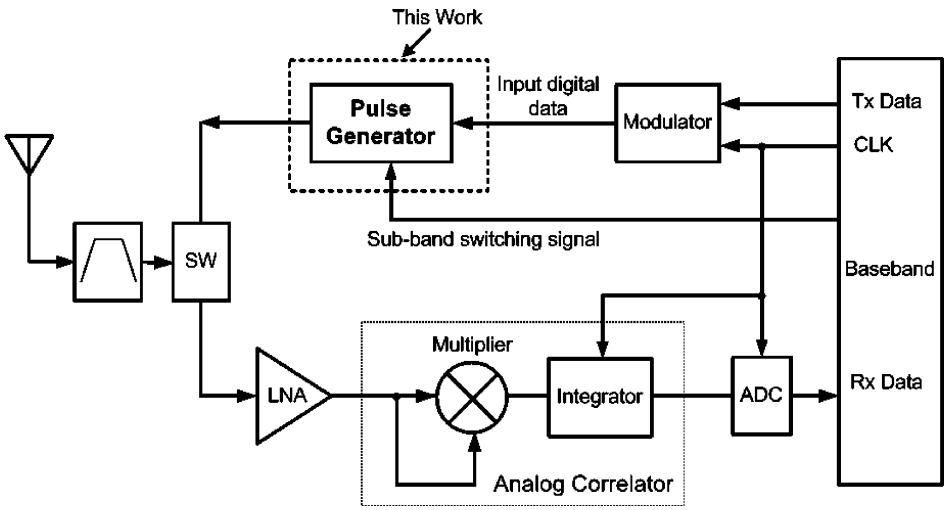

Fig. 1. Proposed low-complexity IR-UWB transceiver architecture for low-data-rate applications.

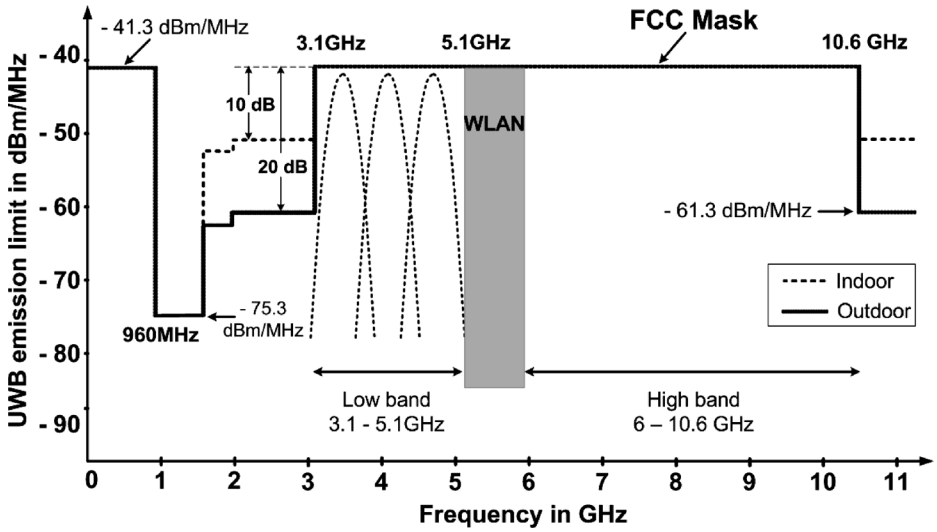

Fig. 2. FCC spectral mask for outdoor and indoor UWB applications.

UWB and narrowband users. To avoid the degradation in the system performance due to such in-band interferences, subband-frequency plan is used for diversity. In the low 3.1–5.1-GHz band shown in Fig. 2, three 528-MHz subbands are proposed. Switching function among these subbands is mandatory for a multiband IR-UWB. For WLAN, 5–6-GHz frequency range is avoided while the high-band spectrum, 6–10 GHz, is reserved for future use. The FCC mask restricts the UWB emission power being under −41.3 dBm/MHz in the ranges of 3.1–10.6 GHz to reduce the potential interferences to existing applications.

As can be seen from the FCC mask shown in Fig. 2, the sidelobe suppression is required to be larger than 20 dB for outdoor system while larger than 10 dB for the indoor system. One of the most significant challenges with pulse-generator design is to meet the FCC spectral mask.

Low dc-power consumption constraint is another demanding factor for designers. In addition, the pulse-generation circuit should be simple and easy to integrate, which enables highly integrated IR-UWB system as a single chip.

So far, there is no regulation for the shape of the UWB pulse waveform as long as the spectral characteristic meets the FCC regulation.

B. Pulse-Generation Schemes and Spectral Characteristics

Previously reported pulse types for IR-UWB system can be categorized into two groups: pulses for single-band and multiband systems.

For the single-band (carrierless) IR-UWB system, the pulse spectrum is designed to occupy the whole allowed 3.1–10.6-GHz frequency band. Therefore, the pulse requires a very short duration (less than a nanosecond) with just one or a few cycles of Gaussian functionlike waveform. Many types of pulses can be the candidates [10], [11], however, to satisfy the wide bandwidth, the Gaussian pulse and its derivatives are preferred, since it contains very small sidelobes and provides a sharp roll-off as compared to other pulse types. The theoretical analysis shows that the higher the derivative order of the Gaussian pulses, the better the roll-off, so the pulse can satisfy the FCC spectral mask

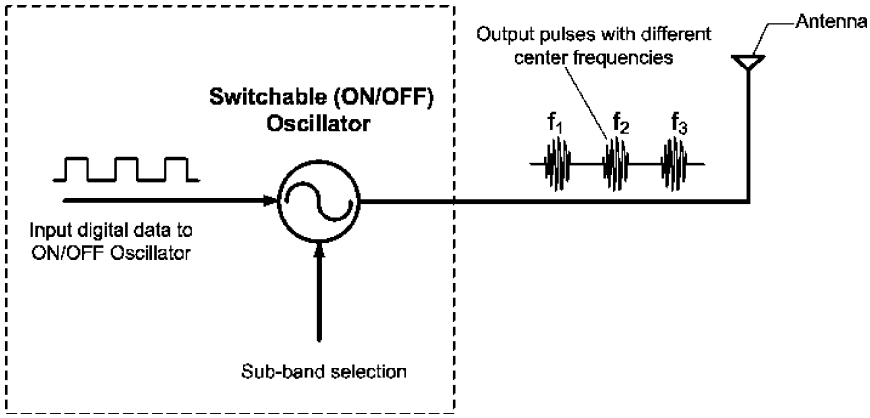

Fig. 3. Pulse-generation principle.

without requiring additional pulse-shaping filters. Analysis in [12] shows that one needs to take at least the seventh derivative to the Gaussian pulse in order to fit the pulse power spectral density (PSD) inside the FCC mask shown in Fig. 2 for the outdoor applications. Considering the order of derivative or the additionally required filter, the Gaussian-pulse-based approach is not recommendable. Furthermore, the high- and the low-frequency components of the PSD do not scale symmetrically as a function of the number of derivatives.

Some of the early pulse generators proposed direct synthesis, using the step-recovery diodes and transmission line [13], [14] or utilizing the BJT characteristic [15]. These types of pulse generators are not easy for integration and not suitable for low-cost and low-complexity implementations. Recently, pulse generators based on analog technique [16]–[19] were presented. In those works, the generated pulses are often the first or second derivatives of Gaussian pulses, which cannot satisfy the FCC mask and, thus, require additional pulse-shaping filter. A digital technique for pulse generation by using pulse pattern generation was reported in [20] with complex circuitry. Moreover, these types of pulse generators consume much higher power, provides no multiband switching, and are complex.

In multiband (carrier-based) IR-UWB systems, the pulse has a longer duration than that of the single-band system and the pulse consists of multiple cycles of sinusoidal waves, thus the bandwidth is smaller for ease of implementation. The multicycle pulses are generated by either combining equally delayed edges [21]–[23] or modulating the amplitude of an oscillator for a specific shape of envelope such as rectangular [24], [25] or triangular [4]. In the former method, the resulting pulse has a center frequency determined by the delay per stage and a pulsewidth which is equal to an integer number of RF cycles determined by the number of edges selected. Thus, a complex circuitry is required for calibration to maintain the delay per stage accurate and equal. In the latter, the center frequency of the oscillator defines the center frequency of the pulse spectrum which should be tunable for the subband switching. Depending on the shape of the pulse envelope, the pulse spectrum shows different characteristics. According to [26], the triangular enveloped pulse can provide a good sidelobe suppression of 26 dB, while only 13 dB can be obtained with rectangular envelope. The amount of sidelobe-suppression factor is important for the multiband system in order to avoid the adjacent channel interferences. For the best performance, the shape of the pulse should be symmetric in time domain, so that its spectrum is concentrated symmetrically around the center frequency with the largest amount of equal sidelobe suppression.

In [4], a pulse is created by multiplying a triangular envelope with a local-oscillator (LO) output. This approach provides a sidelobe suppression of around 20 dB. However, the complexity, a number of functional blocks including a phase-locked loop (PLL), makes it less attractive due to the large chip size and high dc-current consumption. Another way to generate the multiband pulse is to gate an oscillator as proposed in [24]. The problem with this technique is that the envelope of the output pulse is a square shape. Therefore, an additional filtering is required for the sidelobe rejection. It is also power consuming due to the LO operation at the center frequency of pulse spectrum.

III. Pulse-Generation Principle

Fig. 3 shows the pulse-generation principle, in which the multiband pulses are created by the internal switching (on/off) operation of an oscillator. The applied signals for on/off switching are the modulated input digital data. By varying the oscillation frequency, subband center frequency, the subband hopping can be achieved. The output pulse envelope, which determines the pulse spectral characteristics, will be analyzed in the following.

The pulse-generation scheme shown in Fig. 3 will be analyzed by using an *LC*-tank-based oscillator which is adopted for the on/off switching operation. Fig. 4 shows the equivalent circuit of the *LC* oscillator when the oscillator is turned on Fig. 4(a) and turned off Fig. 4(b). In Fig. 4, the L and C represent the resonant tank, R_T the equivalent parasitic resistance of the *LC* tank, $-R$ the negative resistance provided by the active devices, and R_D overall the equivalent resistance of the *LC* tank during the turn-off period.

Assuming a differential *LC* oscillator, the current i_S provided by $-R$ can be represented by a nonlinear polynomial in which the even-order products are cancelled. For simplicity, i_S can be approximated up to third-order nonlinear function of output voltage v_{OUT}

$$i_S = a v_{\mathrm{OUT}} + b v_{\mathrm{OUT}}^3 \tag{1}$$

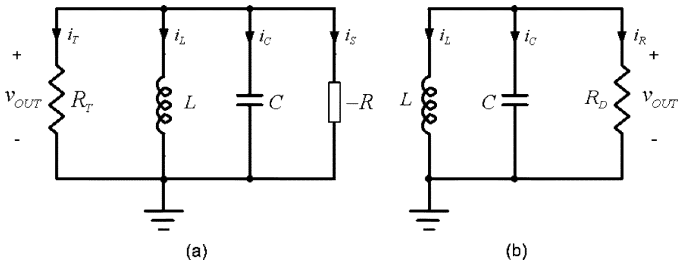

Fig. 4. Equivalent circuits of the *LC* oscillator when the oscillator is (a) turned on and (b) turned off.

where a and b are the first- and third-order coefficients, respectively. The a in (1) represents the linear part of the negative transconductance of the active devices. From Fig. 4(a)

$$i_S + i_L + i_C + i_T = 0. \tag{2}$$

By differentiating (2) with the time, the following differential equation can be obtained:

$$C\frac{\mathrm{d}^2 v_{\mathrm{OUT}}}{\mathrm{d}t^2} + \left(a + 3bv_{\mathrm{OUT}}^2 + \frac{1}{R_T}\right)\frac{\mathrm{d}v_{\mathrm{OUT}}}{\mathrm{d}t} + \frac{v_{\mathrm{OUT}}}{L} = 0. \tag{3}$$

From (3), v_{OUT} can be given by [27]

$$v_{\mathrm{OUT}} = \frac{V_{\mathrm{peak-steady}}}{\sqrt{1+\mathrm{e}^{-(t-t_0)(A_{\mathrm{OL}}-1)\omega_0/Q}}}\cos(\omega_0 t + \phi_0) \tag{4}$$

where $V_{\mathrm{peak-steady}} = \sqrt{4/3[(A_{\mathrm{OL}}-1)/bR_T]}$ is the steady-state peak voltage, $\omega_0 = \sqrt{1/LC}$ is the oscillator resonant frequency, $A_{\mathrm{OL}} = aR_T$ is the open-loop gain, $Q = R_T\sqrt{C/L}$ is the quality factor of the tank, and t_0 and ϕ_0 are the initial values for time and phase, respectively. Equation (4) represents the output voltage waveform of the oscillator as a function of time including the start-up transients. From (4), it can be seen that the oscillator output waveform consists of two components, the oscillation at ω_0 and the envelope part, which is shown in Fig. 5 (the turn-on period). In Fig. 5, which is built to illustrate the pulse-generation principle, the waveform confined with solid line represents the combination of the turn-on and turn-off transients of the oscillator output, while the dashed part represents the oscillator output to the continuous steady-state operation.

Since the envelope of the pulse determines its spectral characteristic, it is useful to obtain the functional dependence of the envelope as a function of design parameters. From Fig. 5, for the turn-on part of the pulse, during the start-up phase, the output voltage swing is small [27], thus the envelope part in (4) can be approximated as

$$v_{\mathrm{env-rise}} = 2V_{\mathrm{peak-steady}}\mathrm{e}^{(t-t_0)(A_{\mathrm{OL}}-1)\omega_0/2Q} \tag{5}$$

where $v_{\mathrm{env-rise}}$ represents the voltage envelope of the output waveform during the turn-on period.

From (5), the required time for a given output envelope voltage can be given by

$$t = \ln\left(\frac{v_{\mathrm{env-rise}}}{v_{\mathrm{env-rise},0}}\right)\left(\frac{2Q}{\omega_0}\times\frac{1}{A_{\mathrm{OL}}-1}\right) \tag{6}$$

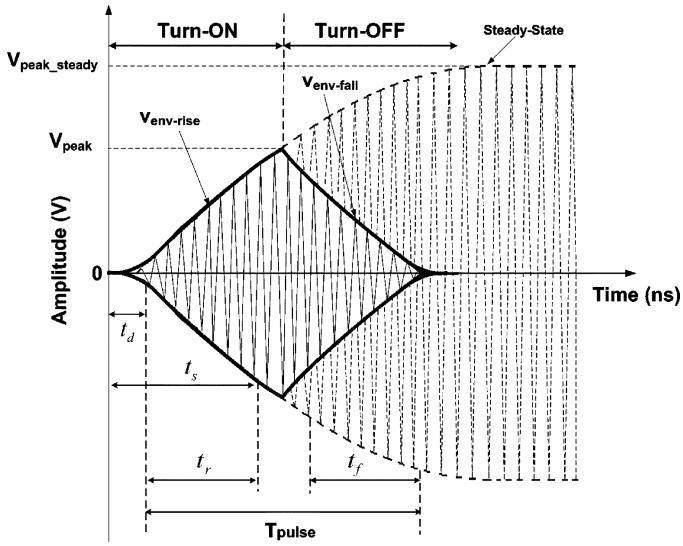

Fig. 5. Illustration of oscillator output waveforms. (Confined with solid line) Turn-on and turn-off transients. (Dashed part) Steady-state output.

where $v_{\mathrm{env-rise},0}$ is the envelope voltage at $t = 0$, which can be the amplitude of the intrinsic thermal noise signal (on the order of nanovolts) for the *LC* tank at the time of start-up. From (5), the relation between $v_{\mathrm{env-rise},0}$ and t_0 can be expressed as

$$t_0 = \ln\left(\frac{2V_{\mathrm{peak-steady}}}{v_{\mathrm{env-rise},0}}\right). \tag{7}$$

$V_{\mathrm{peak-steady}}$ depends on the open-loop gain (A_{OL}) and Q, which is well known and can be found in [27]. The initial start-up is the moment the digital signal triggers the pulse generator by turning on the bias current. With the trigger, the initial condition $v_{\mathrm{env-rise},0}$ is reinforced with a large bias current, which is much greater than the thermal noise [28]. Therefore, from (7), t_0 is reduced significantly as compared to the case of a conventional *LC* oscillator. Once t_0 is known, the absolute values of the delay and the settling times t_d and t_s can be calculated. From (6), t_d and t_s, the time that the output voltages reach 10% and 90% of the peak voltage (V_{peak}), respectively, can be found by setting $v_{\mathrm{env-rise}} = 0.1\ V_{\mathrm{peak}}$ and $0.9\ V_{\mathrm{peak}}$, respectively, such that the rise time t_r can be calculated as

$$t_r = t_s - t_d \approx 4.39\frac{Q}{(A_{\mathrm{OL}}-1)\omega_0} = 4.39\frac{1}{(A_{\mathrm{OL}}-1)}\times CR_T. \tag{8}$$

The bandwidth of the pulse is inversely proportional to its duration. Therefore, the rise time t_r which is supposed to be slightly less than half of the pulse duration (T_{pulse} in Fig. 5) should be in the range of a nanosecond for more than 500 MHz of bandwidth. Equation (8) indicates that small Q and high A_{OL} will help to reduce t_r. Since A_{OL} is also proportional to Q, both t_d and t_r can be reduced effectively by increasing the transconductance of the active devices, which typically requires higher dc current. Thus, achieving nanosecond range of rise time can be a challenge depending on the amount of power dissipation and technology.

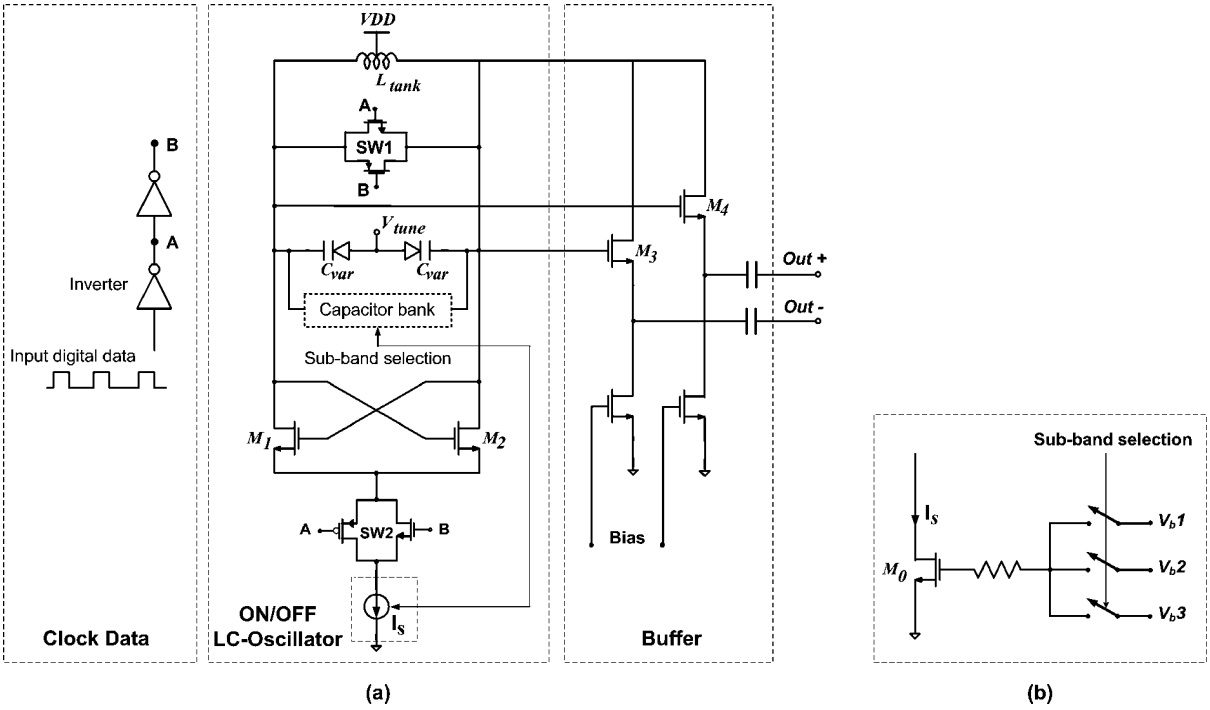

Fig. 6. (a) Proposed pulse-generator circuit schematic. (b) Bias control of current source I_s simultaneously with subband selection.

In Fig. 5, the second half of the pulse consists of the turn-off transient output of the oscillator. To formulate the turn-off transient output waveform, the equivalent circuit shown in Fig. 4(b) can be used. In Fig. 4(b), the equivalent circuit consists of an *LC* tank in parallel with a resistor R_D. During the turn-off transient, the oscillator operation is analogous to a damped oscillation with initial amplitude $V_{\rm peak}$. Applying the well-known damped-oscillation analysis, the output waveform can be given by

$$v_{\rm out} = V_{\rm peak} {\rm e}^{-t/\tau} \cos(\omega_d t + \phi_d) \tag{9}$$

where $\tau = 2CR_D$ is the time constant, $\omega_d = \sqrt{1/LC - 1/\tau^2}$ is the decaying oscillation frequency, and ϕ_d is the initial phase. With weak damping, typically, the time constant τ is much larger than the period of *LC* resonant frequency such that $\omega_d \simeq \omega_0$. From (9), the falling envelope $(v_{\rm env-fall})$ of the oscillator can be given by

$$v_{\rm env-fall} = V_{\rm peak} {\rm e}^{-t/\tau}. \tag{10}$$

From (10), the amount of time for pulse envelope output amplitude to reduce to an arbitrary value $v_{\rm out}$ is given by

$$t = \tau \ln \frac{V_{\rm peak}}{v_{\rm out}}. \tag{11}$$

As shown in Fig. 5, the fall time t_f is defined as the amount of time the envelope amplitude reduces from 90% to 10% of its peak value which can be given by

$$t_f \approx \tau \ln 9 = 4.39 CR_D. \tag{12}$$

Equation (12) indicates that, for the given values of t_r, as the value of C would be determined, the fall time t_f can be controlled by varying R_D only.

As discussed in Section II-B, in order to obtain symmetric pulse spectrum with maximum sidelobe suppression, the fall and rise times of the pulse shown in Fig. 5 should be equal. From (8) and (12), the condition to make $t_r = t_f$ is given by

$$R_D = \frac{R_T}{A_{\rm OL} - 1}. \tag{13}$$

With typical monolithic *LC* tanks, the value of R_T tends to be dominated by the quality factor of the on-chip inductor. Therefore, from (13), since $R_T \geq R_D$, $A_{\rm OL}$ has to be greater than or equal to two. For $A_{\rm OL} > 2$, R_D has to be smaller than R_T, which means that the *LC* tank requires an additional shunt resistor during the turn-off period.

IV. Pulse-Generator Design

A. Pulse-Generator Topologies

Fig. 6 shows the proposed circuit schematic of a pulse generator based on the switching on/off of an *LC* oscillator. As shown in Fig. 6, the core circuit of the pulse generator consists of a multiband, by adopting capacitor bank, conventional differential VCO, and a couple of transmission gate switches along with inverters to obtain complementary clock from the input digital data for switch control. The use of inverter also helps sharpen the rising/falling edge of clock signal.

The fundamental idea shown in Fig. 6 is to create the pulse signal shown in Fig. 5 by turning on and off the oscillator using the switches. The oscillation can be turned on and off by switching one of the two switches in Fig. 6, SW1 or SW2. For the case of using SW1 only, the pulse generator dissipates a constant dc power which is not an optimum option as a low-power solution. The other option is to use SW2 only,

which can satisfy the dual purposes of power saving and oscillation switching. By adopting SW2 only, the power dissipation can be reduced significantly as the pulse generator dissipates dynamic current only without static current. The amount of power dissipation will be proportional to the data rate due to the inversely proportional duty cycle. For the case of adopting SW2 only, from (13), the open-loop gain of the oscillator $A_{\rm OL}$ has to be exactly equal to two as R_D in Fig. 4(b) becomes R_T. In this case, from (12), the value of the tank capacitor C and the quality factor of the inductor (determines the value of R_T) have to be adjusted to satisfy the required amount of fall time. For a 2-nH inductor with Q-factor of ten in a typical CMOS technology, R_T is calculated as 500 Ω at 4 GHz (C has to be equal to 0.79 pF). From (12), t_f is 1.74 ns, which is slightly longer than the required fall time for the 500-MHz bandwidth. For $R_D = R_T$, (12) can be reexpressed as

$$t_f \approx 4.39 C R_T \propto \frac{Q}{\omega_0}. \tag{14}$$

From (14), since the inductor dominates the Q-factor of the *LC* tank, the reduction in fall time t_f can be achieved by adopting the lower Q inductor. The inductor Q-factor can be reduced by thinning the metal width of the on-chip spiral which will lead to the smaller size inductor. One possible complication of the pulse generator using only SW2 is that the reduction in Q-factor of the inductor could lead to too small output power, in which case, an additional (wideband) amplifier might be needed. The requirement of an additional amplifier could spoil the original motivation of low-power pulse generator.

Now, the third option is adopting both switches in Fig. 6, where SW2 is used for power-saving purpose only and SW1 for the control of fall time without reducing the output power. The two switches operate alternately; when one switch is on, the other is off and vice versa. With adoption of SW1, the R_D in Fig. 4(b) becomes equal to $R_T//R_{\rm sw1}$, where $R_{\rm sw1}$ is the on-resistance of the SW1. By the proper selection of $R_{\rm sw1}$, the fall time t_f can be controlled without affecting the Q-factor of the *LC* tank and $A_{\rm OL}$. Therefore, the output power can be controlled independently without affecting the fall time.

B. Circuit Implementation and Variation Consideration

The pulse generator shown in Fig. 6(a) with dual switch has been adopted as a final architecture for the implementation. The adopted architecture dissipates no static current but only the dynamic current. The combination of SW1 and SW2 gives more design flexibility in controlling the pulse shape and the corresponding PSD.

In Fig. 6(a), the input digital data, supplied from the modulator, controls the two switches for the pulse generation. The inverters in Fig. 6(a) create the complementary signals (nodes A and B) for the two switches. The first inverter is adopted to suppress the possible concurrent noise in the baseband signal, providing cleaner complementary signal at nodes A and B. The complementary signal from nodes A and B are applied to the two switches with 180° of phase difference.

As discussed in the previous section, the pulse PSD depends on the pulse envelope which is determined by the transconductance of active devices of the VCO, the switching transistor size, Q-factor of the *LC* tank, and the tank capacitance. Therefore, by the proper selection of these four parameters which have been described and analyzed in Section III, the desired pulse envelope can be obtained. The active transistors M1,2 have a width/length (W/L) ratio of 40 μm/0.18 μm. A high-biased current source (I_s) can be used without concerning of power consumption to provide sufficient g_m and output amplitude, since I_s is turned on only during the pulse emission. For the rest of a cycle, which is much longer than the pulse duration in a low-duty-cycle operation ($\sim$1%), I_s is turned off, resulting in a very small average power dissipation. Minimum channel length is used for SW1 with a width/length $(W/L)_1$ ratio of 50 μm/0.18 μm and 25 μm/0.18 μm for nMOS and pMOS transistors, respectively. Thus, the on-resistance of SW1 is in the range of a few 10 Ω. The size of SW1,2 is selected based on the simulation for optimal PSD with highest amount of sidelobe suppression. $(W/L)_2$ ratio is 50 μm/0.18 μm and 40 μm/0.18 μm for nMOS and pMOS transistors, respectively.

Since the pulse generator will directly drive the antenna, a buffer is cascaded after the pulse generator to isolate the oscillator core from the load impedance variation and for measurement. Thus, the oscillation is not affected by the load and more stable. The source-follower topology is adopted in the buffer for 50-Ω load impedance with proper sizing and bias. When the 50- Ω wideband antenna is driven [29]–[32], the original output pulse shape and its PSD will be preserved and not change significantly due to the broadband characteristic of the UWB antenna.

The bonding wire and pad are included to take into account their effects during the simulation. Bonding inductance and bond pad capacitance are the most dominant factors. Typical bonding wire of 1 mm is used which introduces about 0.8 nH of inductance. Signal pad is designed with the top metal layer to reduce parasitic capacitance. By varying the length of bonding wire, we experience that the output pulse is not sensitive to the change of bonding wire.

As discussed in Section III, the center frequency of the generated pulse is mainly determined by the oscillation frequency of the VCO. In the proposed pulse generator, the subband switching of the pulse spectrum is achieved by varying the resonant frequency of the *LC* tank using the switched capacitor bank [30]. As the pulse center frequencies are switched among subbands, the pulse PSDs experience around 1.5 dB of variation in magnitude and slightly change in bandwidth. This variation is due to the changes of Q-factor and tank capacitance at different frequencies. The peak values of pulse PSD can be adjusted to be equal by controlling I_s, the turn-on bias current of the pulse generator shown in Fig. 6(b). The bias voltage for M_0 to generate I_s is varied with different values $(V_{\rm b}1{-}3)$ for each respective subband, resulting in $\pm$5% tuning range of I_s. Subband selection signal is used to choose the right bias current and corresponding subband simultaneously.

Fig. 7 shows the simulated pulse PSDs of the proposed pulse generator over the three subbands of 3–5-GHz range. The three subbands, centered at 3.5, 4, and 4.5 GHz, respectively, show equal PSD levels with 528-MHz bandwidth. They fully comply with FCC spectral mask and can be extended further to operate in UWB high band.

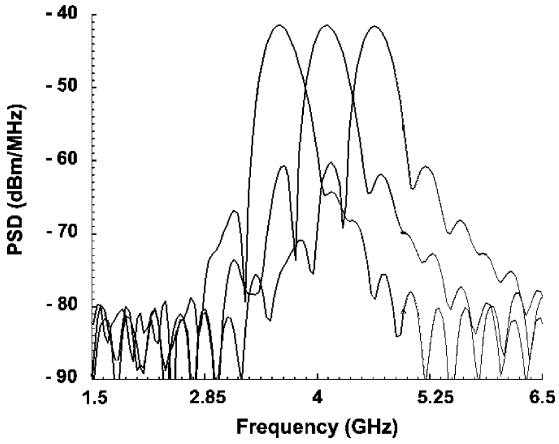

Fig. 7. Simulated PSD of the designed pulse-generator output over the three subbands in 3–5-GHz range.

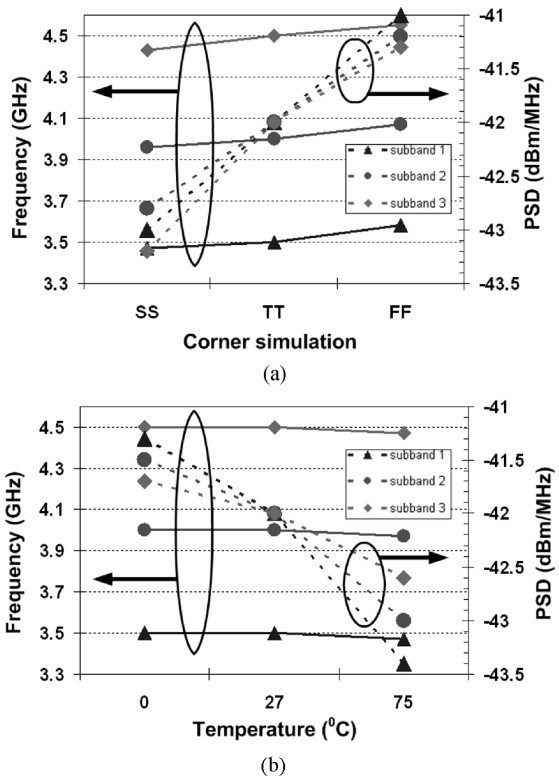

Fig. 8. Simulation results of pulse center frequency and PSD for three subbands as a function of (a) process by corner simulation and (b) temperature.

The pulse-spectrum center frequency and magnitude may be varied due to process and temperature dependence. Simulations results of center frequency and PSD magnitude as a function of process and temperature for the three subbands are shown in Fig. 8. To verify the process variation, corner simulation is performed in three modes (SS, TT, FF) at 27 °C. From Fig. 8(a), corner simulations show that pulse center frequencies are varied about 1.5% due to the process. As for temperature changes from 0 °C to 75 °C in typical operation condition (TT), shown in Fig. 8(b), pulse center frequencies show a slight variation of less than 0.5%. It could be tolerable in UWB system, since the frequency variation is relatively small as compared to a subband

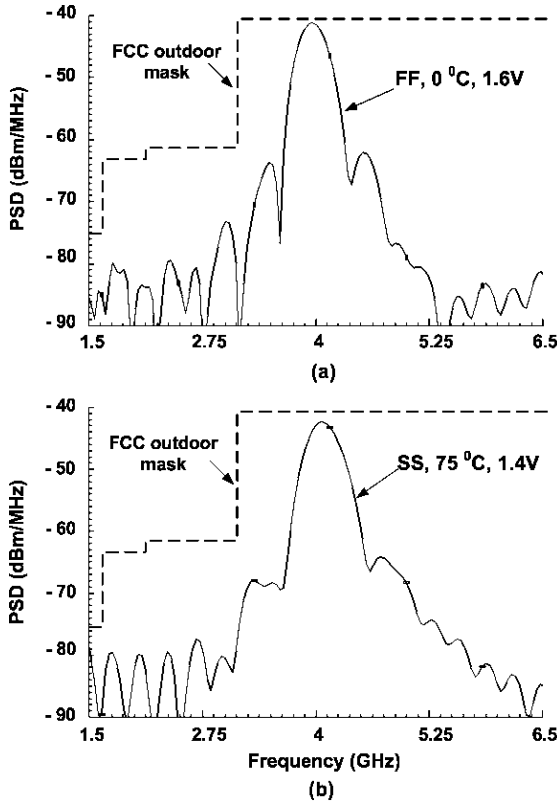

Fig. 9. Simulated PSDs of the output pulse as compared with FCC spectrum mask for the two extreme cases. (a) FF, 0 °C, 1.6 V and (b) SS, 75 °C, 1.4 V.

bandwidth of more than 500 MHz. Furthermore, the pulse center frequency can be tuned using the varactors with Vtune in the same manner as in wideband conventional VCO design [33]. Vtune is used for fine tuning only during the measurement in energy-detection (ED) noncoherent system, since the frequency selection is not strictly required. As for the coherent system, however, Vtune is necessary when the time-shared PLL [34] is adopted. The fine tuning range is about 150 MHz, which is sufficient to combat with the variation.

Shown in Fig. 8, the pulse PSD magnitudes are varied by the same amount of 2 dB due to both process and temperature dependences. By regulating I_s as aforementioned, however, equal PSD levels can be obtained as shown in Fig. 7.

When the rise and fall times are varied due to PVT, the pulse's PSD is also affected. From (8) and (14), the ratio of t_r/t_f can be expressed as

$$\frac{t_r}{t_f} = \frac{R_T/R_{\rm sw1}+1}{A_{\rm OL}-1}. \tag{15}$$

R_T may vary due to the change in Q-factor and center frequency, so does $R_{\rm sw1}$ due to PVT. From (15), in order to maintain the ratio of t_r/t_f, which is supposed to be equal, $A_{\rm OL}$ can be tuned by varying the bias current I_s.

Fig. 9 shows the impact of PVT variation on the spectrum of the output pulse, which is due to the changes in rise and fall times. The two extreme cases with FF mode (low threshold voltage) at 0-°C 1.6-V supply and SS mode (high threshold voltage) at 75-°C 1.4-V supply are shown in Fig. 9(a) and (b), respectively. In both cases, the pulse's PSDs are still compliant

with FCC mask when the rise and fall times undergo PVT variation without any tuning. Thus, the PSD is robust against PVT variation.

Another concern is that the spectral bandwidth of a subband also varies due to the changes in rise and fall times. However, the minimum bandwidth is still greater than 500 MHz. The pulse spectral bandwidth can be controlled by varying the duration of the input digital data, which partly determines the duration of the pulse (T_{pulse}).

The limitation of the proposed pulse-generation technique is the lack of accurate control over the center frequency. The conventional PLL cannot be applied due to the switching operation of the pulse generator. However, it may be possible to lock the pulse oscillation frequency by adopting the aforementioned time-shared PLL [34], a power-saving switching PLL, at the cost of additional power dissipation and chip size. Moreover, the proposed pulse generator is designed for ED, a noncoherent system, which is shown in Fig. 1. In the ED receiver [35], a squarer is used to collect pulse energy and convert to dc by using an integrator [7] or a low-pass filter [36]. Then, the output of integrator is compared with noise level of the environment through a comparator to detect the presence or absence of input pulses. Thus, pulse-amplitude information is more desirable, which is required to be high enough above the noise level. The accuracy requirement of pulse center frequency is much relaxed and makes the proposed pulse generator well suited for ED receivers. Therefore, the drawback of the proposed pulse generator is outnumbered by the advantages of low-power consumption, high spectral characteristic performance, and low complexity.

V. Measurement Results

To verify the proposed idea, a single-band pulse generator is implemented following the proposed dual-switch architecture as described earlier. The implemented pulse generator is designed for 1.5-V supply based on a 0.18-μm CMOS technology. Fig. 10 shows the simulated and measured output pulse waveforms of the implemented pulse generator where a 3.5-ns-duration digital data is applied as an input. The simulation and measurement results (at single output) are in good agreement. The maximum peak-to-peak amplitude of the measured pulse is 160 mV, which is high enough for transmission without requiring additional wideband amplification. In Fig. 10, the pulse envelope shows an acceptable symmetry with relatively close rise and fall times, leading to a triangularlike shape, which ensures high spectral characteristics with large amount of sidelobe suppression as discussed earlier.

The delay time t_d, which is calculated from the start-up moment to 10% of the pulse peak, is measured as 0.5 ns. Fig. 11 shows the output pulse train measured at the pulse repetition frequency (PRF) of 100 MHz or a pulse period of 10 ns. Each pulse is generated for the duration of 3.5 ns over every 10 ns. Maximum pulse rate, which is limited by pulse duration to avoid overlapping, may reach over 200 MHz.

Since the magnitude of PSD is proportional to PRF, one may vary the PRF to adjust the PSD to meet FCC mask for a given pulse amplitude. Fig. 12 shows the pulse PSD of the generated pulse measured at a PRF of 40 MHz. It is shown in Fig. 12 that the center frequency of the pulse is 3.8 GHz, the same as the VCO oscillation frequency, and the bandwidth is 520 MHz

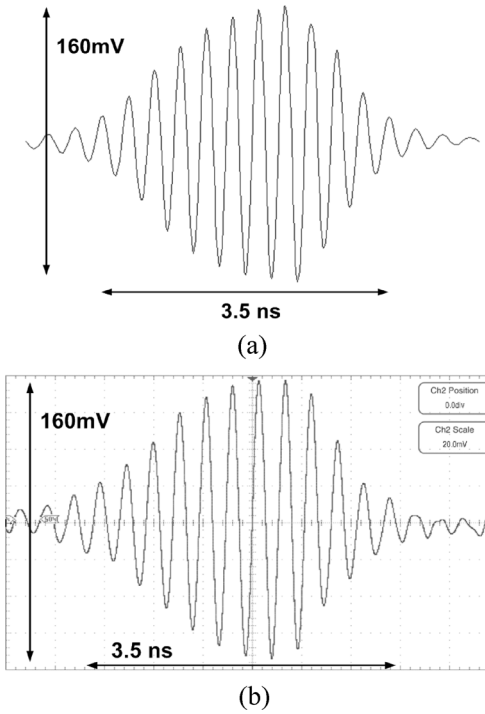

Fig. 10. (a) Simulated and (b) measured output pulse waveforms.

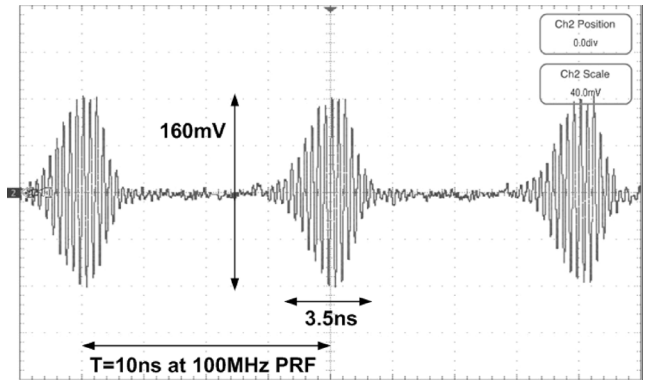

Fig. 11. Measured output pulse train at 100 MHz of PRF.

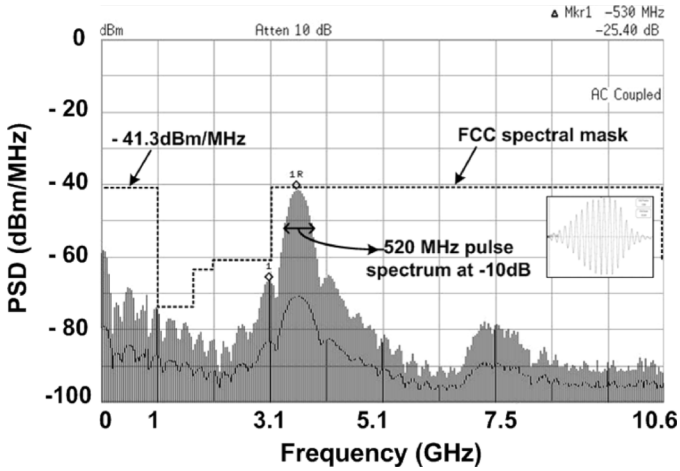

Fig. 12. Measured pulse PSD in compliance with FCC mask.

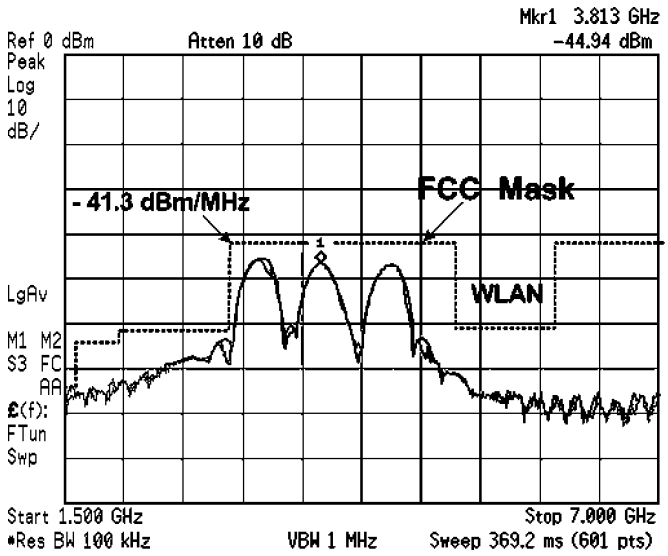

Fig. 13. PSD of three 528-MHz subbands in compliance with FCC mask [37].

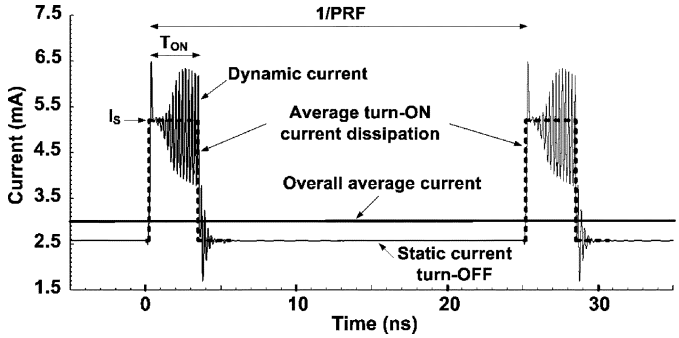

Fig. 14. Transient simulation of current dissipation of the pulse generator during turn-on and turn-off.

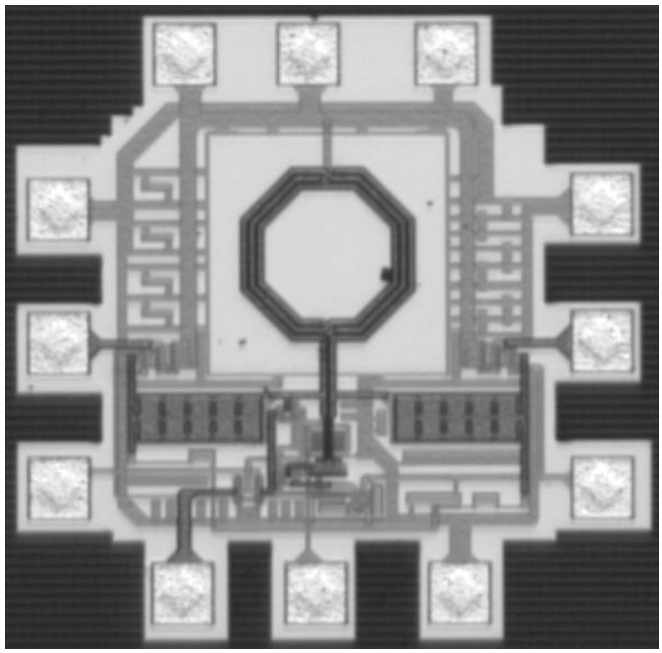

Fig. 15. Chip photograph of the implemented pulse generator.

which is slightly smaller than the 528 MHz. Following the convention, the bandwidth is measured at 10 dB below the peak power level. In Fig. 12, the peak power (marked "1R") and the amount of sidelobe suppression (difference between marks "1" and "1R") are measured as −41.3 dBm and 25 dB, respectively. The measured pulse spectrum fully fits under FCC mask in the whole UWB band from dc to 10.6 GHz, and the sidelobe suppression is higher than the required 20 dB with margin without requiring any additional filtering circuitry. Therefore, the pulse generator can maintain its low complexity for low-cost low-power goal.

A complete IR-UWB OOK transmitter adopting the proposed pulse-generation principle with three subbands operating in 3–5-GHz range is reported in [37]. The subband switching function of the pulse generator is implemented by varying the resonant frequency of the *LC* tank using the switched capacitor bank as aforementioned. The measured PSD of the three subbands in 3–5-GHz range is shown Fig. 13.

The proposed pulse generator dissipates only the dynamic current from the 1.5-V supply. The buffer dissipates 2.6 mA of a static current. Its current source might also be gated on/off by the same clock signal as for the core circuit to reduce the baseline power dissipation. As a result, the buffer is enabled only during the pulse emission and disabled when there is no pulse transmission to remove unwanted power consumption. The transient of current dissipation of the pulse generator during turn-on and turn-off is shown in Fig. 14. During the turn-on, the dynamic current dissipation can be approximated as a square current pulse (dash line) with the peak value of I_s and a $T_{\rm ON}$ (3.5 ns) for average power-consumption calculation. During the turn-off, the circuit consumes only static current.

The dynamic current of the proposed pulse generator proportionally depends on the PRF of the pulse train. At different PRFs of 100 kHz, 20 MHz, and 100 MHz, the dynamic currents are estimated as 1.13, 225, and 1120 μA, respectively. Thus, the energy consumption per pulse is roughly the same amount of 16.8 pJ, which is well suited for low-power solution.

TABLE I
SUMMARY OF THE MEASURED PULSE-GENERATOR PERFORMANCE

Parameters	Measured Results
Sub-band center frequency	3.8 GHz
Bandwidth	520 MHz
Peak power spectral density (PSD)	– 41.3 dBm/MHz
Maximum sidelobe suppression	> 25 dB
V_{pp}	160 mV
Pulse duration	3.5 ns
Dynamic current at PRF of 0.1, 20, and 100 MHz	1.13, 225, and 1120 µA, respectively.
Energy consumption per pulse [+]	~ 16.8 pJ
V_{DD}	1.5 V
Chip size	560 x 550 µm^2
Technology	CMOS 0.18-μm

[+] Excluding the output buffer power consumption.

TABLE II
PERFORMANCE COMPARISON OF THE PROPOSED PULSE GENERATOR WITH PREVIOUSLY PUBLISHED WORKS

References	Pulse Type	Technology	Output Vpp	Pulse width/BW	Power Cons. (pJ/pulse)
[16], 2006	mono-cycle	CMOS 0.18μm	800 mV	250 MHz	700
[40], 2006	mono-cycle	SiGe BiCMOS	170 mV	175 ps	132
[21], 2007	mono-cycle	CMOS 0.13μm	350 mV	0.7 ns/2 GHz	30
[13], 2002	1st derivative Gaussian	Discrete, SRD	400 mV	300 ps	n.a
[6], 2006	2nd derivative Gaussian	CMOS 0.18μm	~30 mV	<1 ns/1.5 GHz	21 (mW) for Tx *
[38], 2005	5th derivative Gaussian	CMOS 0.5μm	148 mV	2.4 ns	~58
[4], 2005	multi-cycle	CMOS 0.18μm	200 mV	1.1 – 4.5 ns	50
[41], 2006	multi-cycle	CMOS 0.18μm	900 mV	~2 ns	180
[39], 2006	multi-cycle	BiCMOS 0.18μm	200 mV	550 MHz	252
[20], 2007	multi-cycle	CMOS 0.18μm	640 m V	1.75 ns	29.7 (mW) for Tx *
[19], 2005	Edge combine and shaping filter	CMOS 0.18μm	~160 mV	0.5 ns	4 (Simulation)
[22], 2006	Delay cell shapping	CMOS 0.09μm	900 mV	7 GHz/from 22-29 GHz	1.4
[23], 2007	Delay cell shapping	CMOS 0.09μm	650 mV	600 MHz	47
This work	**multi-cycle**	**CMOS 0.18μm**	**160 mV**	**3.5 ns/ 520 MHz**	**16.8** +

* The total power consumption of the transmitter (Tx).
+ Excluding the output buffer power consumption.

Fig. 15 shows the die microphotograph of the fabricated pulse generator. The total chip size including all the bonding pads is $820 \times 810\ \mu\text{m}^2$ while the core size is $560 \times 550\ \mu\text{m}^2$.

Table I summarizes the performance of the implemented pulse generator and Table II shows comparison with various previously reported pulse generators. In Table II, the energy consumption per pulse is calculated as a figure-of-merit for the comparison of energy efficiency. The proposed pulse generator shows an excellent value of energy consumption per pulse among other reported works. It means that the proposed pulse generator can transmit data efficiently with a longer battery life.

VI. CONCLUSION

In this paper, the design, analysis, and implementation of an ultralow-power low-complexity pulse-generation technique for multiband IM-UWB system have been presented. The on/off switching operation of an oscillator is adopted to generate pulses in response to the input digital data. Three different ways to switch the *LC* oscillator have been considered, and their advantages and limitations in the aspects of power consumption and spectral performance are analyzed. From the analysis, an oscillator with dual switch, one for the *LC* tank and the other for the current source, has been proposed as the final architecture for the pulse generator. The proposed architecture has been verified with the implementation of a single-subband pulse generator, which can easily be extended to multiple subbands in 3.1–5.1-GHz range. The design parameters that determine the pulse envelope of proposed pulse generator, which depends on the rise and fall times of the envelope, are analyzed and provided with the guidelines. As a result, triangularlike enveloped pulses are achieved, and its PSD completely satisfies FCC spectral mask and shows more than 25 dB of sidelobe suppression without any extrafiltering. Implemented in a 0.18-μm CMOS technology from 1.5-V supply, the pulse generator is compact and highly integrated with the core die size of 0.3 mm^2. It consumes only the burstlike dynamic current which is proportional to the PRF. Excellent energy efficiency is achieved with the energy dissipation per pulse of roughly 16.8 pJ. Since the output pulse is triggered by the input digital data, the proposed pulse generator can accommodate both pulse position and OOK-modulated signals.

The implemented pulse generator is well suited for the ED scheme (noncoherent) IR-UWB system, which promises a low-cost low-power low-complexity impulse radio.

ACKNOWLEDGMENT

The authors would like to thank I. N. Yeom from Tektronix Korea, Ltd., for his kind assistance in providing measurement equipment.

REFERENCES

[1] *"Revision of Part 15 of the Commission's Rules Regarding Ultra-Wideband Transmission Systems: First Report and Order,"* |Federal Communications Commission, Washington, DC, 2002, ET-docket 98-153, FCC 02-48.

[2] L. Stoica, S. Tiuraniemi, A. Rabbachin, and I. Oppermann, "An ultra wideband tag circuit transceiver architecture," in *Proc. Joint Ultra Wideband Syst. Technol. Conf.*, Kyoto, Japan, May 2004, pp. 258–262.

[3] I. Oppermann, L. Stoica, A. Rabachin, Z. Shelby, and J. Haapola, "UWB wireless sensor networks: UWEN—A practical example," *IEEE Commun. Mag.*, vol. 42, no. 12, pp. S27–S32, Dec. 2004.
[4] J. Ryckaert, C. Desset, A. Fort, M. Badaroglu, V. De Heyn, P. Wambacq, G. Van der Plas, S. Donnay, B. Van Poucke, and B. Gyselinckx, "Ultra-wide-band transmitter for low-power wireless body area networks: Design and evaluation," *IEEE Trans. Circuits Syst. I, Reg. Papers*, vol. 52, no. 12, pp. 2515–2525, Dec. 2005.
[5] IEEE 802.15 Task Group 4a [Online]. Available: http://www.ieee802.org/pub/15/TG4a.html
[6] Y. Zheng, Y. Zhang, and Y. Tong, "A novel wireless interconnect technology using impulse radio for interchip communications," *IEEE Trans. Microw. Theory Tech.*, vol. 54, no. 4, pt. II, pp. 1912–1920, Jun. 2006.
[7] L. Stoica, A. Rabbachin, and I. Oppermann, "A low-complexity noncoherent IR-UWB transceiver architecture with TOA estimation," *IEEE Trans. Microw. Theory Tech.*, vol. 54, no. 4, pt. II, pp. 1637–1646, Jun. 2006.
[8] Y. Zheng, Y. Tong, J. Yan, Y.-P. Xu, W. G. Yeoh, and F. Lin, "A low power noncoherent CMOS UWB transceiver ICs," in *Proc. IEEE RFIC*, Jun. 2005, pp. 347–350.
[9] C. W. Kim, M. S. Kang, P. T. Anh, H. T. Kim, and S.-G. Lee, "An ultra-wideband CMOS low noise amplifier for 3–5-GHz UWB system," *IEEE J. Solid-State Circuits*, vol. 40, no. 2, pp. 544–547, Feb. 2005.
[10] X. Chen and S. Kiaei, "Monocycle shapes for ultra wideband system," in *Proc. IEEE ISCAS*, May 2002, vol. 1, pp. 597–600.
[11] W. T. Ang, J. Chen, and T. Lv, "High-order monocycle design and its waveform-generating circuit for UWB communications," *IEEE Trans. Circuits Syst. I, Reg. Papers*, vol. 54, no. 8, pp. 1657–1665, Aug. 2007.
[12] H. Sheng, P. Orlik, A. M. Haimovich, L. J. Cimini, and J. Zhang, "On the spectral and power requirements for ultra-wideband transmission," in *Proc. IEEE ICC*, May 2003, vol. 1, pp. 738–742.
[13] J. Han and C. Nguyen, "A new ultra-wideband, ultra-short monocycle pulse generator with reduced ringing," *IEEE Microw. Wireless Compon. Lett.*, vol. 12, no. 6, pp. 206–208, Jun. 2002.
[14] J. Han and C. Nguyen, "On the development of a compact sub-nanosecond tunable monocycle pulse transmitter for UWB applications," *IEEE Trans. Microw. Theory Tech.*, vol. 54, no. 1, pp. 285–293, Jan. 2006.
[15] J. F. M. Gerrits and J. R. Farserotu, "Wavelet generation circuit for UWB impulse radio applications," *Electron. Lett.*, vol. 38, no. 25, pp. 1737–1738, Dec. 2002.
[16] T. Terada, S. Yoshizumi, M. Muqsith, Y. Sanada, and T. Kuroda, "A CMOS ultra-wideband impulse radio transceiver for 1-Mb/s data communications and ± 2.5-cm range finding," *IEEE J. Solid-State Circuits*, vol. 41, no. 4, pp. 891–898, Apr. 2006.
[17] S. Bagga, W. A. Serdijin, and J. R. Long, "A PPM Gaussian monocycle transmitter for ultra-wideband communications," in *Proc. Joint Ultra Wideband Syst. Technol. Conf.*, Kyoto, Japan, May 2004, pp. 130–134.
[18] Y. Jeong, S. Jung, and J. Liu, "A CMOS impulse generator for UWB wireless communication systems," in *Proc. IEEE ISCAS*, May 2004, vol. 4, pp. 129–132.
[19] B. Jung, Y.-H. Tseng, J. Harvey, and R. Harjani, "Pulse generator design for UWB IR communication systems," in *Proc. IEEE ISCAS*, May 23–26, 2005, pp. 4381–4384.
[20] T. Norimatsu, R. Fujiwara, M. Kokubo, M. Miyazaki, A. Maeki, Y. Ogata, S. Kobayashi, N. Koshizuka, and K. Sakamura, "A UWB-IR transmitter with digitally controlled pulse generator," *IEEE J. Solid-State Circuits*, vol. 42, no. 6, pp. 1300–1309, Jun. 2007.
[21] L. Smaini, C. Tinella, D. Helal, C. Stoecklin, L. Chabert, C. Devaucelle, R. Cattenoz, N. Rinaldi, and D. Belot, "Single-chip CMOS pulse generator for UWB systems," *IEEE J. Solid-State Circuits*, vol. 41, no. 7, pp. 1551–1561, Jul. 2006.
[22] A. Oncu, M. Fujishima, T. Wang, and B. B. M. Wasanthamala Badalawa, "22–29 GHz CMOS pulse generator for ultra-wideband radar application," in *Proc. IEEE ESSCIRC*, Sep. 2006, pp. 279–282.
[23] D. D. Wentzloff and A. P. Chandrakasan, "A 47 pJ/pulse 3.1-to-5 GHz all-digital UWB transmitter in 90 nm CMOS," in *IEEE Int. Solid-State Circuits Conf.*, Feb. 2007, pp. 118–119.
[24] Y. H. Choi, "Gated UWB pulse signal generation," in *Proc. IEEE Joint Int. Workshop UWBST IWUWBS*, May 2004, pp. 122–124.
[25] A. Azakkour, M. Regis, F. Pourchet, and G. Alquie, "A new integrated monocycle generator and transmitter for ultra-wideband (UWB) communications," in *Proc. IEEE RFIC Symp.*, Jun. 2005, pp. 79–82.
[26] J. Ryckaert, M. Badaroglu, C. Desset, V. De Heyn, G. van der Plas, P. Wambacq, B. van Poucke, and S. Donnay, "Carrier-based UWB impulse radio: Simplicity, flexibility, and pulser implementation in 0.18-micron CMOS," in *Proc. IEEE Int Conf. Ultra-Wideband*, Sep. 2005, pp. 432–437.
[27] J. T. van der, D. Kasperkovitz, and A. van Roermund, *High-Frequency Oscillator Design for Integrated Transceivers*. Boston, MA: Kluwer, 2003.
[28] A. Rusznyak, "Start-up time of CMOS oscillators," *IEEE Trans. Circuits Syst.*, vol. CAS-34, no. 3, pp. 259–268, Mar. 1987.
[29] S. Bagga, A. Vorobyov, S. Haddad, A. G. Yarovoy, W. A. Serdijin, and J. R. Long, "Codesign of an impulse generator and miniaturized antennas for IR-UWB," *IEEE Trans. Microw. Theory Tech.*, vol. 54, no. 4, pp. 1656–1666, Jun. 2006.
[30] J. Lee, Y. Park, M. Kim, C. Yoon, J. Kim, and K. Kim, "System-on-package ultra-wideband transmitter using CMOS impulse generator," *IEEE Trans. Microw. Theory Tech.*, vol. 54, no. 4, pp. 1667–1674, Jun. 2006.
[31] S. B. T. Wang, A. M. Niknejad, and R. W. Brodersen, "Circuit modeling methodology for UWB omnidirectional small antennas," *IEEE J. Sel. Areas Commun.*, vol. 24, no. 4, pp. 871–877, Apr. 2006.
[32] P. K. Datta, X. Fan, and G. Fischer, "A transceiver front-end for ultra-wide-band applications," *IEEE Trans. Circuits Syst. II, Exp. Briefs*, vol. 54, no. 4, pp. 362–366, Apr. 2007.
[33] A. D. Berny, A. M. Niknejad, and R. G. Meyer, "A 1.8-GHz *LC* VCO with 1.3-GHz tuning range and digital amplitude calibration," *IEEE J. Solid-State Circuits*, vol. 40, no. 4, pp. 909–917, Apr. 2005.
[34] N. Joehl, C. Dehollain, P. Favre, P. Deval, and M. Declerq, "A low-power 1-GHz super-regenerative transceiver with time-shared PLL control," *IEEE J. Solid-State Circuits*, vol. 36, no. 7, pp. 1025–1031, Jul. 2001.
[35] S. Dubouloz, B. Denis, S. Rivaz, and L. Ouvry, "Performance analysis of LDR UWB noncoherent receivers in multipath environments," in *Proc. IEEE Int. Conf. Ultra Wideband*, Sep. 2005, pp. 491–496.
[36] S. R. Duenas, X. Duo, S. Yamac, M. Ismail, and L.-R. Zheng, "CMOS UWB IR noncoherent receiver for RF-ID applications," in *Proc. IEEE North-East Workshop Circuits Syst.*, Jun. 2006, pp. 213–216.
[37] T.-A. Phan, J. Lee, V. Krizhanovskii, S.-K. Han, and S.-G. Lee, "A 18 pJ/pulse OOK CMOS transmitter for multiband UWB impulse radio," *IEEE Microw. Wireless Compon. Lett.*, vol. 17, no. 9, pp. 688–690, Sep. 2007.
[38] H. Kim and Y. Joo, "Fifth-derivative Gaussian pulse generator for UWB system," in *Proc. IEEE RFIC*, Jun. 2005, pp. 671–674.
[39] D. D. Wentzloff and A. P. Chandrakasan, "Gaussian pulse generators for subbanded ultra-wideband transmitters," *IEEE Trans. Microw. Theory Tech.*, vol. 54, no. 4, pt. II, pp. 1647–1655, Apr. 2006.
[40] A. E. Tan, M. Y. Chia, and S. Leong, "Sub-nanosecond pulse-forming network on SiGe BiCMOS for UWB communications," *IEEE Trans. Microw. Theory Tech.*, vol. 54, no. 3, pp. 1019–1024, Mar. 2006.
[41] D. D. Barras, F. Ellinger, H. Jackel, and W. Hirt, "Low-power ultra-wideband wavelets generator with fast start-up circuit," *IEEE Trans. Microw. Theory Tech.*, vol. 54, no. 5, pp. 2138–2145, Mar. 2006.

Anh Tuan Phan (A'07) was born in Hanoi, Vietnam, in 1979. He received the B.S. degree in electronics and telecommunication from Hanoi University of Technology, Hanoi, in 2002 and the M.Sc. and Ph.D. degrees in electrical engineering from Information and Communications University (ICU), Daejeon, Korea, in 2004 and 2008, respectively.

He is currently a Postdoctor with the μ-Radio Laboratory, ICU. His current research interests include CMOS RFIC design, UWB radio transceiver design, and low-power low-cost circuit solutions.

Jeongseon Lee was born in Jinju, Korea, in 1969. She received the B.S. degree in electric and electronics engineering from Korea Advanced Institute of Science and Technology, Daejeon, Korea, in 1992 and the M.S. and Ph.D. degrees in information and communications from Gwangju Institute of Science and Technology, Gwangju, Korea, in 1997 and 2005, respectively.

She is currently a research staff with μ-Radio Laboratory, Information and Communications University, Daejeon. Her main research interests include radio-frequency integrated circuit.

Vladimir Krizhanovskii was born in Donetsk, Ukraine, in 1978. He received the Specialist degree in radiophysics and electronics from Donetsk State University, Donetsk, in 2000. He is currently working toward the Ph.D. degree in electrical engineering in the μ-Radio Laboratory, Information and Communications University, Daejeon, Korea.

His current research interests include direct-conversion receiver design and ultrawideband impulse-radio receiver design.

Quan Le received the B.Sc. and M.Sc. degrees in physics and radio electronics from Hanoi National University, Hanoi, Vietnam, in 1996 and 2000, respectively, and the Ph.D degree in electrical engineering from Information and Communications University, Daejeon, Korea, in 2006.

Since 2006, he has been with the Electronics and Telecommunications Research Institute, Daejeon, where he has been developing burst-mode receiver ICs for gigabit passive optical network (GPON). His research interest includes CMOS radio-frequency integrated circuit design and 2.5- and 10-Gbit/s burst-mode receiver for GPON and Ethernet PON future standards.

Seok-Kyun Han was born in Cheonnam, Korea, in 1964. He received the B.S. degree in electronic engineering from Kwangju University, Kwangju, Korea, in 1995, the M.S. degree in electrical engineering from Mokpo University, Mokpo, Korea, in 1998, and the Ph.D. degree in electrical engineering from Mokpo Maritime University, Mokpo, in 2004.

Since 2004, he has been with μ-Radio Laboratory, Information and Communications University, Daejeon, Korea, where he is currently a Research Assistant Professor. His research interests include silicon-technology-based radio-frequency integrated circuit and microwave circuits design.

Sang-Gug Lee (M'05) was born in Gyungnam, Korea, in 1958. He received the B.S. degree in electronic engineering from Gyungbook National University, Daegu, Korea, in 1981 and the M.S. and Ph.D. degrees in electrical engineering from the University of Florida, Gainesville, in 1989 and 1992, respectively.

In 1992, he joined Harris Semiconductor, Melbourne, FL, where he was engaged in silicon-based radio-frequency integrated-circuit designs. From 1995 to 1998, he was an Assistant Professor with the School of Computer and Electrical Engineering, Handong University, Pohang, Korea. Since 1998, he has been with μ-Radio Laboratory, Information and Communications University, Daejeon, Korea, where he is currently a Full Professor. His research interests include the silicon-technology-based (BJT, BiCMOS, CMOS, and SiGe BICMOS) radio-frequency integrated-circuit (IC) designs such as LNA, mixer, oscillator, power amp, etc. He is also active in the high-speed IC designs for the optical communication such as transimpedance amp, driver amp, limiting amp, etc.